



Technology Development for Thick Section of Aerospace-Grade MDN 250 Weldment with Higher Weld Strength and Toughness by Suppressing Reverted Austenite Phase

Bibin Jose, Manikandan Manoharan , and Arivazhagan Natarajan

Submitted: 6 June 2021 / Revised: 18 September 2021 / Accepted: 21 September 2021 / Published online: 18 October 2021

Maraging steels are precipitation hardened steels with high-strength and excellent toughness. Maraging steels being the key player in the strategic sector, demands welding of thick sections up to 12 mm for critical applications. They are readily weldable in the soft solution-annealed condition and further strengthened by post-weld heat-treatment (PWHT). However, welding of thick sections, on the other hand, necessitates a longer welding time, more number of passes and a higher heat input. This paper elucidates the influence of different PWHTs on the metallurgical and mechanical behavior of 12-mm-thick plates of MDN 250 grade maraging steel by using multi-pass gas metal-arc welding (GMAW). The different PWHTs adopted for the study include; Direct Aging (DA), Solutionizing + Aging (SA) and Homogenizing + Solutionizing + Aging (HSA). The microstructures of the fusion zone (FZ) with DA and SA condition reveal the presence of reverted austenite (RA) along the cell boundaries. However, in the weldment with HSA treatment was free from RA. Metallographic analysis of the as-welded FZ showed nickel, molybdenum and titanium segregation along the cell boundaries. This resulted in the formation of RA on subsequent aging. The SA treatment was not effective in complete elimination of reversion. The HSA treatment, on the other hand, had completely eliminated both elemental segregation and reversion. The welded joint with HSA treatment had an ultimate tensile strength (UTS) of 1582 MPa and a fracture toughness of 92.9 MPa√m, respectively. HSA treatment also shows a remarkable improvement in fracture toughness compared to other PWHTs. The present study underscores the fact that multi-pass GMAW with HSA treatment provides optimal mechanical properties.

Keywords aging, fracture toughness, homogenizing, MDN-250, reverted austenite, solutionizing

1. Introduction

Maraging steels are a type of martensitic steels, which are renowned for their exceptional high-strength and outstanding toughness. This rare blend of mechanical properties has made it a preferred choice for critical applications in defense and aerospace sectors (Ref 1). Maraging steels derive its strength from the age-hardening reaction of martensite. They are highly alloyed materials that contain elements like nickel, molybdenum, titanium and aluminum as their major constituents (Ref 2, 3). In comparison to conventional steels, maraging steel has a very low carbon content. As the presence of carbon is considered as an impurity element in maraging steels. Maraging steel shows flexibility in most manufacturing processes like machining, forming, welding and so on. The exceptional feature of being weldable in the solution-annealed condition

followed by post-weld aging at a comparatively lower temperature makes these steels well-suited for the fabrication of large structures (Ref 4). From the welding point of view, arc welding received more attention in a wide range of applications (Ref 5). Apart from this, electron beam welding (Ref 6-8), friction stir welding (Ref 9-11) and laser beam welding (Ref 12-14) were successful in joining thin-sheets to moderately thick plates (~ 6 mm). However, as plate thickness increases, achieving a very low edge-gap and a precise joint fit-up becomes more difficult. Conventionally, welding of thick sections are carried out by using the multi-pass gas tungsten arc welding (GTAW) processes. Gupta et al. (Ref 15) performed comparative studies on GTAW and plasma arc welding (PAW) of an 8-mm-thick plate of MDN 250 grade maraging steel. It was observed that the filler wire consumption for PAW was one-fifth that of GTAW. The tensile test results for the weld produced using PAW were 3-4% higher than those employed by GTAW. Further, the fracture toughness results of PAW were comparable to those of GTAW. Subashini et al. (Ref 16) performed single-pass laser-gas metal-arc hybrid welding (LHW) on a 10-mm-thick plate of maraging steel (MDN-250). The test results showed a weld efficiency of 97.3% and fracture toughness of 77.4 MPa√m in the aged condition. In a similar study, Subashini et al. (Ref 4) compared single-pass LHW and double-sided laser welding of 10-mm-thick plates of maraging steel (MDN-250). Laser welding showed higher tensile strength and higher FZ hardness compared to LHW. However, as compared to laser welding, LHW showed 57% improvement in

Bibin Jose, Manikandan Manoharan, and Arivazhagan Natarajan, School of Mechanical Engineering, Vellore Institute of Technology, Vellore, Tamil Nadu, India. Contact e-mails: mano.manikandan@gmail.com and bibinjose96@gmail.com.

Table 1 The chemical compositions (wt.%) of base material and filler wire

Elements	C	Ni	Co	Mo	Ti	Al	P	Si	Fe
MDN 250	0.004	18.91	7.75	4.91	0.47	0.112	0.01	0.01	Bal.
Filler wire W2	0.002	18.07	11.8	2.5	0.17	0.42	0.003	0.02	Bal.

fracture toughness. It is to be noted that there are a few papers available in the published literature that address the weldability of thick section, with sample thickness up to 10 mm (Ref 4, 15, 16). Additionally, the effect of different PWHTs on mechanical properties of thick sections of MDN 250 weldment has not been reported elsewhere. The defense and aerospace sectors are demanding joints with higher thickness; for example, critical applications like the rocket motor casings involve welding of sections greater than 10 mm. As the thickness increases, GMAW can produce joints with fewer passes than GTAW in a lesser time. In this respect, the possibility of welding thick sections by GMAW cannot be ruled out.

The primary concern, when welding maraging steel is the formation of RA (Ref 7, 18). RA is a decomposition product, which is formed on aging Fe-Ni martensite (Ref 17). During welding, micro-segregation of alloying elements like Ni, Mo and Ti in the inter-dendritic regions of the FZ lowers the austenite start temperature. This eventually leads to the formation of RA during its subsequent aging. Such reversions in the FZ were noticed by different researchers. For example, Fanton et al. (Ref 19) reported it in MDN 300 grade weldments. Shamantha et al. (Ref 20), Madhusudhan Reddy et al. (Ref 21) and Venkateswara Rao et al. (Ref 22) reported RA in MDN 250 weldments. It is observed that the presence of RA reduces hardness, strength and toughness of the FZ (Ref 18). The presence of RA can be reduced or eliminated by the use of optimized W2 filler wire and the use of suitable PWHTs (Ref 20-23). But, the influence of different PWHTs on mechanical behavior is not clear so far. It is also interesting to note that no recent studies have been carried out in GMAW which is considered as the cheapest and most reliable technique in welding. To date, no comprehensive analysis has been conducted that addresses the role of different PWHT in the microstructure and mechanical behavior of MDN 250 grade maraging steel using GMA welding. This present research work explores the possibility of multi-pass GMA welding on 12-mm-thick plates and also the effect of various PWHTs on the microstructural and mechanical behavior of MDN 250 weldments.

2. Experimental Procedure

2.1 Specimen Preparation and Welding

MDN 250 grade maraging steel plate of 900 mm × 900 mm × 12 mm was brought in the solution-annealed condition from MIDHANI, Hyderabad. The weld coupons were prepared from the as-received plate to the required dimensions of 300 mm × 100 mm × 12 mm using wire-cut electron discharge machining (W-EDM) machine. Acetone was used to clean the plates to

Table 2 Welding parameters

Parameters	Values
Voltage	24 V
Shielding gas (Argon)	15 L/min
Wire Feed	12 , mm/sec
No of passes	7
Average Heat Input	0.76 kJ/mm
Total Heat Input	5.32 kJ/mm

remove any unwanted particles. The filler material adopted in the experiment was an optimized W2 filler of 1.2-mm-diameter which was also procured in the form of a spool from MIDHANI, Hyderabad. The W2 filler has higher Co and Al content but lower Mo and Ti contents compared to the base material. The filler wire chemistry was developed to reduce segregation during welding and subsequent solidification (Ref 20). The chemical compositions (wt.%) of the base metal and filler wire are represented in Table 1. The multi-pass GMAW butt welding was carried out on coupons with V-groove edge preparation. The root face height of 2 mm and an included angle of 60° were machined using a milling machine. During welding, a 1.2-mm-gap was kept between the plates. The samples are clamped tightly to avoid the distortion during the welding process. The welding was performed by a ZUPER ARC 400 MIG welding machine. Bead on trails was carried out to establish the process parameters. The range of process parameters values was selected from the literature (Ref 17). The welding parameters are listed in Table 2.

2.2 Post-Weld Heat-Treatment (PWHT)

The welded coupons are subjected to three different PWHTs, namely –

- (i) Direct aging (480 °C/3h).
- (ii) Solutionizing (815 °C/1h) + aging (480 °C/3h)
- (iii) Homogenizing (1150 °C/1h) + solutionizing (815 °C/1h) + aging (480 °C/3h)

Each stage of PWHTs was followed by air cooling. Further, the different post-weld heat-treated samples were characterized to investigate their effect on microstructure and mechanical behavior.

2.3 Metallurgical Characterization

A W-EDM was used to slice the weldments perpendicular to the weld profile in order to investigate the metallurgical properties. The microstructural specimens were polished as per ASTM E-3 standard. After polishing, the specimens were chemically etched to reveal the microstructure. Fifteen percent

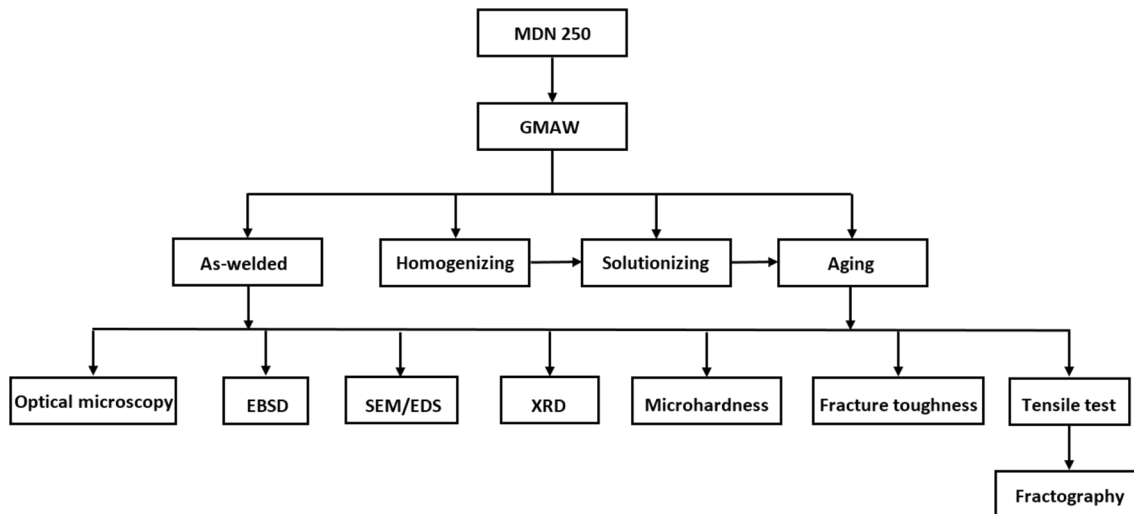


Fig. 1 The overall experimental flow diagram

Nital (15% HNO_3 , 85% Ethanol) was used as the etchant. The macrostructures were captured using “AM4115 T Dino-Lite-Edge microscope”. Microstructural images were taken using a ZEISS optical microscope. A ZEISS scanning electron microscope (SEM) was utilized to capture micro-level features at a higher magnification. The micro-segregation of alloying elements were evaluated using energy dispersive spectroscopy (EDS). To analyze the phases at the FZ, an X-ray diffraction (XRD) tests were performed on a BRUKER D8 advanced device. An EDAX-TSL device connected to a Fei Quanta-3d FE-SEM was used to test electron backscatter diffraction (EBSD). EBSD patterns were analyzed by the OIM software.

2.4 Mechanical Characterization

Transverse tensile tests were carried out as per the ASTM E8 standards. The tests were carried out at a constant strain rate of 2 mm/min and at ambient conditions. Fractography of the samples were performed using SEM. Compact tension (CT) specimens with a straight notch were utilized to evaluate the fracture toughness (K_{Ic}) of the weldments. The test was carried out using the ASTM E399 standard. The input loading conditions for pre-cracking were 0.3 to 3 kN before the initiation of the crack. The load decreased by 0.05 kN and ranged between 0.25 and 2.5 kN followed by the initiation of the crack. The fracture toughness tests were performed at 0.5 kN/s. The Vicker’s microhardness tests were carried out on the weldment cross-section, at an applied load of 500 gf and with a dwell period of 10 s. The overall experimental plan is given in Fig. 1.

3. Results and Discussion

3.1 Macro and Microstructure

3.1.1 Base Metal. The microstructure of MDN 250 grade maraging steel is shown in Fig. 2. The as-received base metal was in the solution-annealed condition, which revealed a



Fig. 2 Microstructure of MDN 250 as-received condition

single-phase lath martensite structure with an average grain size of 10 μm . Maraging steel is produced by heating the steel to the austenitizing temperature which is followed by air cooling. Higher nickel content promotes the formation of lath martensite structure. The Lath martensite structure with its prior austenitic grain boundaries sets up a barrier to dislocation motion, resulting in maraging steel with excellent mechanical properties (Ref 24).

3.1.2 Weld Metal. The multi-pass GMA welding was completed in seven passes. After welding, the samples were subjected to radiographic examinations. The X-ray radiography of the weldments were free from defects. Figure 3 shows a cross-sectional macrograph of maraging steel weldment along with a Fe-Ni phase diagram. The welding of maraging steel witnesses four different zones; the FZ, HAZ 1, HAZ 2 and the base metal. The FZ experiences temperature above 1500 $^{\circ}\text{C}$ which is sufficient to melt the base material. HAZ 1, which is located adjacent to the FZ gets heated to the austenitic phase-field during welding and transforms back to martensite on

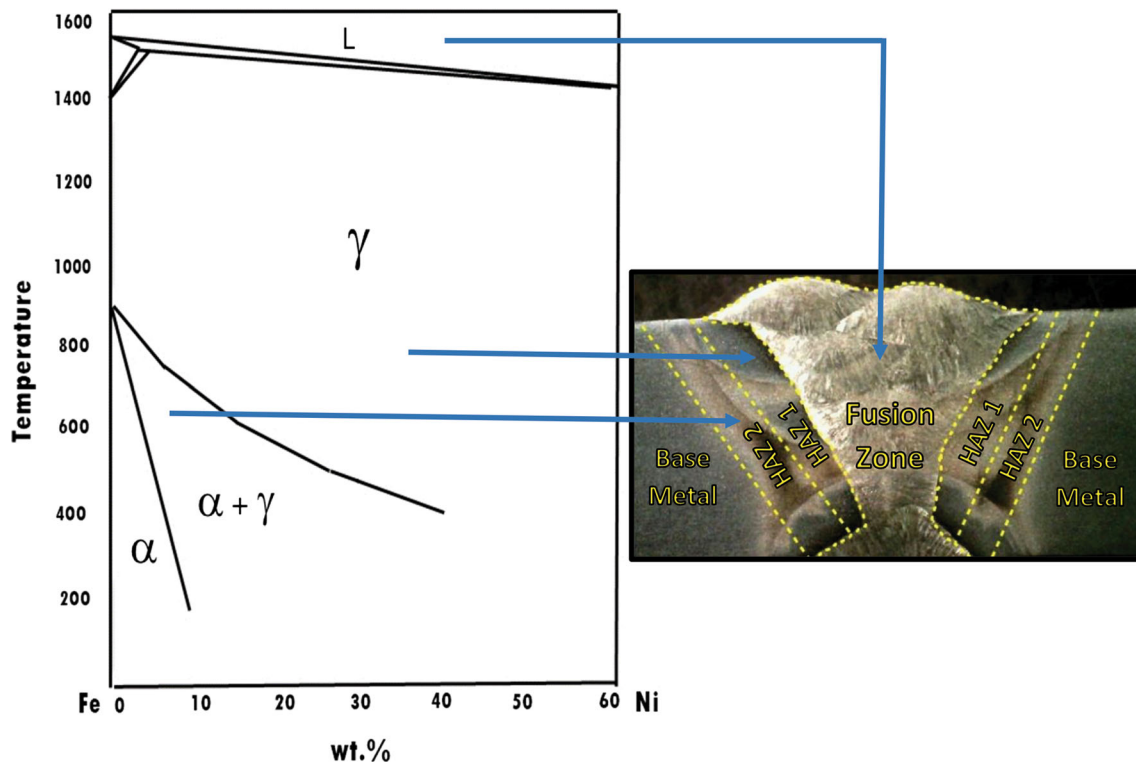


Fig. 3 Temperature distribution at different zones during welding from the Fe–Ni phase diagram

cooling. The temperature experienced in this region is above 1000 °C. HAZ 2 is the dark etched region or is also known as the eyebrow region. It is a two-phase region with martensite and fine dispersion of stable RA. The temperature experienced in the range of 600 °C – 750 °C. The last zone is the base metal region, which is not affected by weld thermal cycle.

Figure 4a-h shows the macro and microstructure of the as-welded samples. Figure 4a shows the macrostructure of the weldment. It is clear that the cross-sectional macrograph is free from defects such as porosity, slag inclusions and cracks. Furthermore, the weld bead shape is almost symmetrical along the fusion centerline with full penetration. The macrostructure depicts the FZ, HAZ 1 and the dark etched HAZ 2.

During welding, the weld-fusion microstructure transforms from austenite to martensite upon cooling to room temperature. Figure 4(b) (c) and f shows the microstructure of three different areas in the FZ namely mid, cap and root pass, respectively. The FZ depicts dendritic morphology in the microstructure. The occurrence of various forms of dendrites (like cellular, columnar and equiaxed dendrites) in the weld FZ solely depends on the rate of cooling. The existence of columnar dendrite depends on “constitutional supercooling”. On the other hand, lower rate of constitutional supercooling favors the formation of cellular dendrites. Columnar dendrites are formed by the directional emergence of new nuclei and dendrite growth along the axis of heat extraction (Ref 25). The grain orientations along the FZ vary according to the temperature gradients. Figure 4 (d) shows the interface of FZ and HAZ 1.

Figure 4 (e), (g) and (h) shows the microstructures of HAZ 1 and HAZ 2. Adjacent to the FZ lays the HAZ 1. It has a lath martensitic structure, which is similar to that obtained in the base metal. Adjacent to the HAZ 1 lays the dark etched HAZ 2.

It consists of martensite structure with a fine dispersion of RA, within the prior austenite grain boundaries. Over-aging during welding causes the formation of RA in HAZ 2 (Ref 26). This RA is too small that optical microscope cannot resolve it.

Figure 5 (a-h) shows the macro and microstructure of the direct aged (DA) condition. Figure 5 (a) shows the macrostructure of the weldment in the DA condition. The macrostructure resembles to that of as-welded condition. Figure 5 (b) (c) and (f) shows the microstructure of mid, cap and root pass. The microstructure predominantly shows cellular and columnar dendritic structure. Figure 5 (d) shows the interface of the FZ and HAZ 1. Figure 5 (e) shows a more magnified image of dendrite. Beneath the dendrite, lath martensite structure is clearly visible. On the dendrite, the bright white color patches represent the RA. A similar observation was reported by several researchers (Ref 21, 22, 26). Figure 5 (g) and (h) shows the microstructure of HAZ 1 and HAZ 2.

Figure 6 (a-h) shows the macro and microstructure of the solutionized + aged (SA) condition. Figure 6 (a) shows the macrostructure of the weldment in the SA condition. The macrostructure reveals FZ and a single HAZ. The solutionizing treatment has eliminated the dark etched zone of the HAZ. In the as-welded condition, the HAZ 2 comprises of martensite with a fine dispersion of stable RA. The post-weld solutionizing treatment at a temperature of 815 °C contributed to a reduction in the presence of austenite content, which in turn completely dissolves the HAZ 2 into the matrix. Figure 6 (b) (c) and (f) shows the microstructure of mid, cap and root pass. The FZ microstructure resembles to that of the DA condition. Figure 6 (d) shows the interface of the FZ and HAZ. Figure 6 (e) shows a more magnified image of the dendrites. The white color patches on the dendrite represents RA as observed in the DA

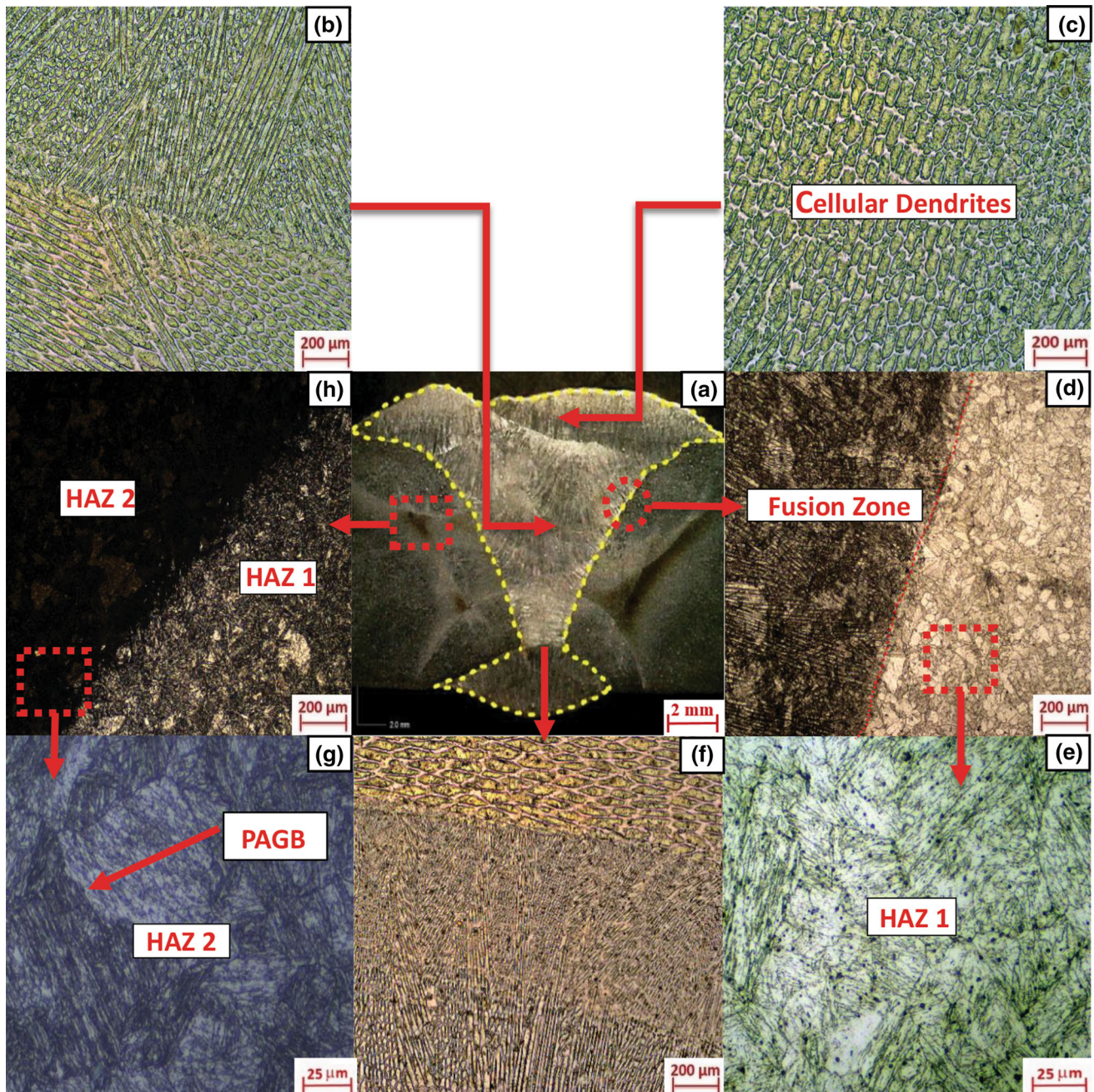


Fig. 4 (a-h) Macro and microstructure of as-welded sample

condition. However, the extent of RA content is less when compared to DA condition. Figure 6 (c) and (g) shows the microstructures of HAZ.

Figure 7 (a-h) shows the macro and microstructure of the homogenized + solutionized + aged (HSA) condition. Figure 7 (a) shows the macrostructure of the weldment with HSA condition. The macrostructure only reveals the FZ. The boundaries of HAZ and the base metal zone disappears. The HAZ has lost its identity after HSA treatments, hence the region adjacent to the FZ is represented as “erstwhile HAZ” region. Figure 7 (b) (c) and (f) shows the microstructure of mid, cap and root pass. The microstructure reveals the absence of

dendritic structure in the FZ. Figure 7 (h) and (g) shows the interface of FZ and erstwhile HAZ. Figure 7 (d) and (e) shows the microstructure of erstwhile HAZ and the base metal. It can be observed in the case of HSA condition both base metal and the erstwhile HAZ look alike.

3.2 Micro-Segregation

The SEM micrographs of the FZ in as-welded and PWHT conditions are given in Figure 8 (a-d). All the images were recorded at a constant magnification of 2000x. The SEM images in the as-welded, DA and SA conditions depict the

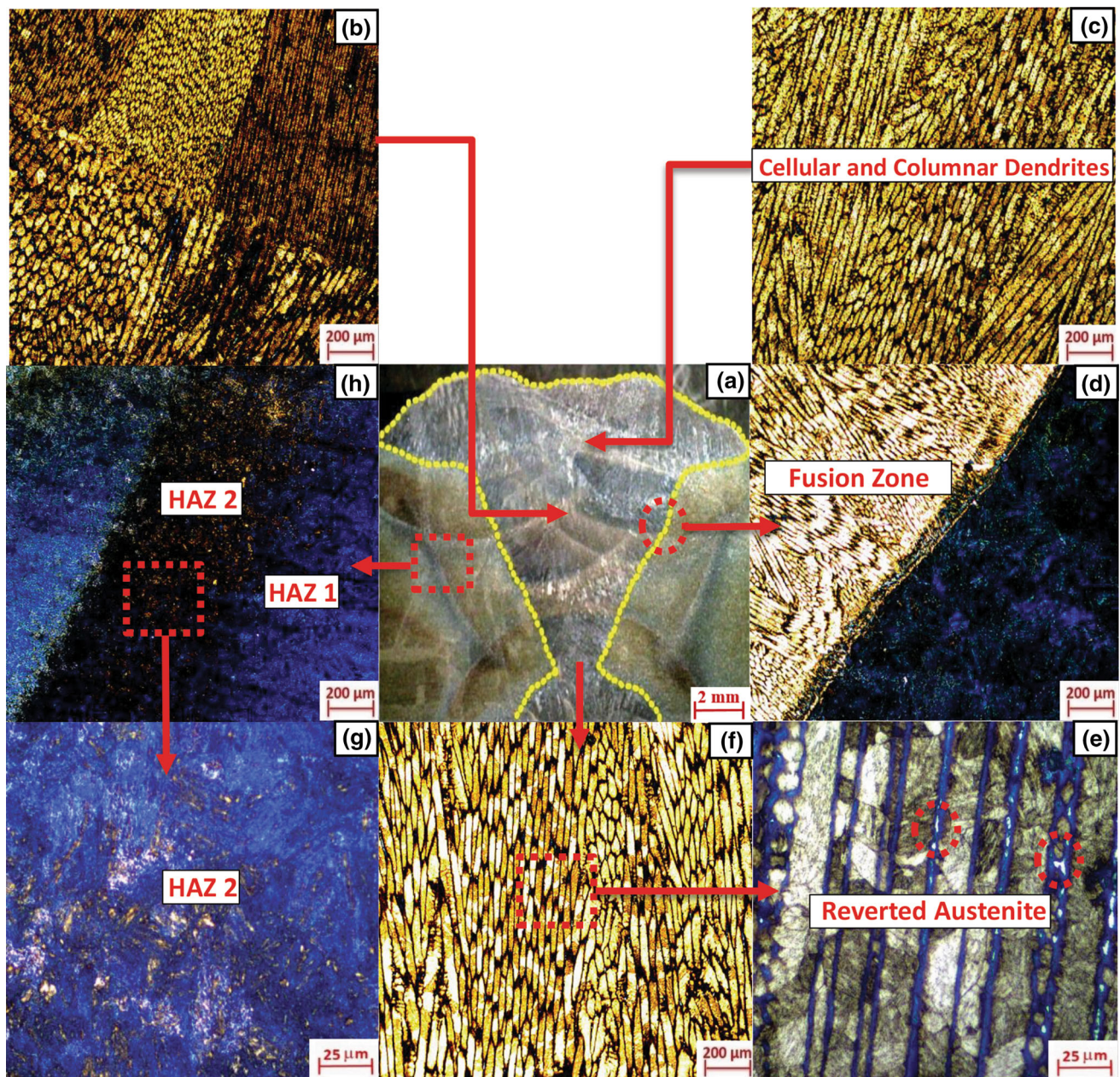


Fig. 5 (a-h) Macro and microstructure of DA condition

dendritic morphologies, whereas the presence of dendrite is absent in HSA condition. The elemental composition at the cell center and cell boundary regions were analyzed through SEM-based EDS analysis. Table 3 shows the elemental composition at the cell center and cell boundary regions of as-welded and different PWHT conditions. In all the conditions except HSA, the EDS point mapping at cell boundary is labeled as “(i)”, and cell center is labeled as “(ii)”. In the case of HSA due to the absence of dendrites, EDS point mapping were randomly taken from different points, of which two are mentioned in the table. It can be seen that the segregation of nickel, molybdenum and titanium from the cell center to cell boundaries is observed in

the as-welded condition. However, the extent of segregation of cobalt and aluminum was not observed. The micro-segregation of alloying elements during welding lowers the A_s (austenite start) temperature. This eventually leads to the formation of austenite phase during its subsequent aging. These austenite phases are thermally stable at room temperature. The austenite so formed is generally termed as RA. From the EDS analysis, it is clear that the segregation effect is more pronounced in cell boundaries, rather than the cell center. Due to this fact, the RA was formed on the dendritic cell boundary as observed from the microstructure. Similar observations were reported by Li et al. [23] in laser welding and Rao et al. (Ref 22) in GTA welding of

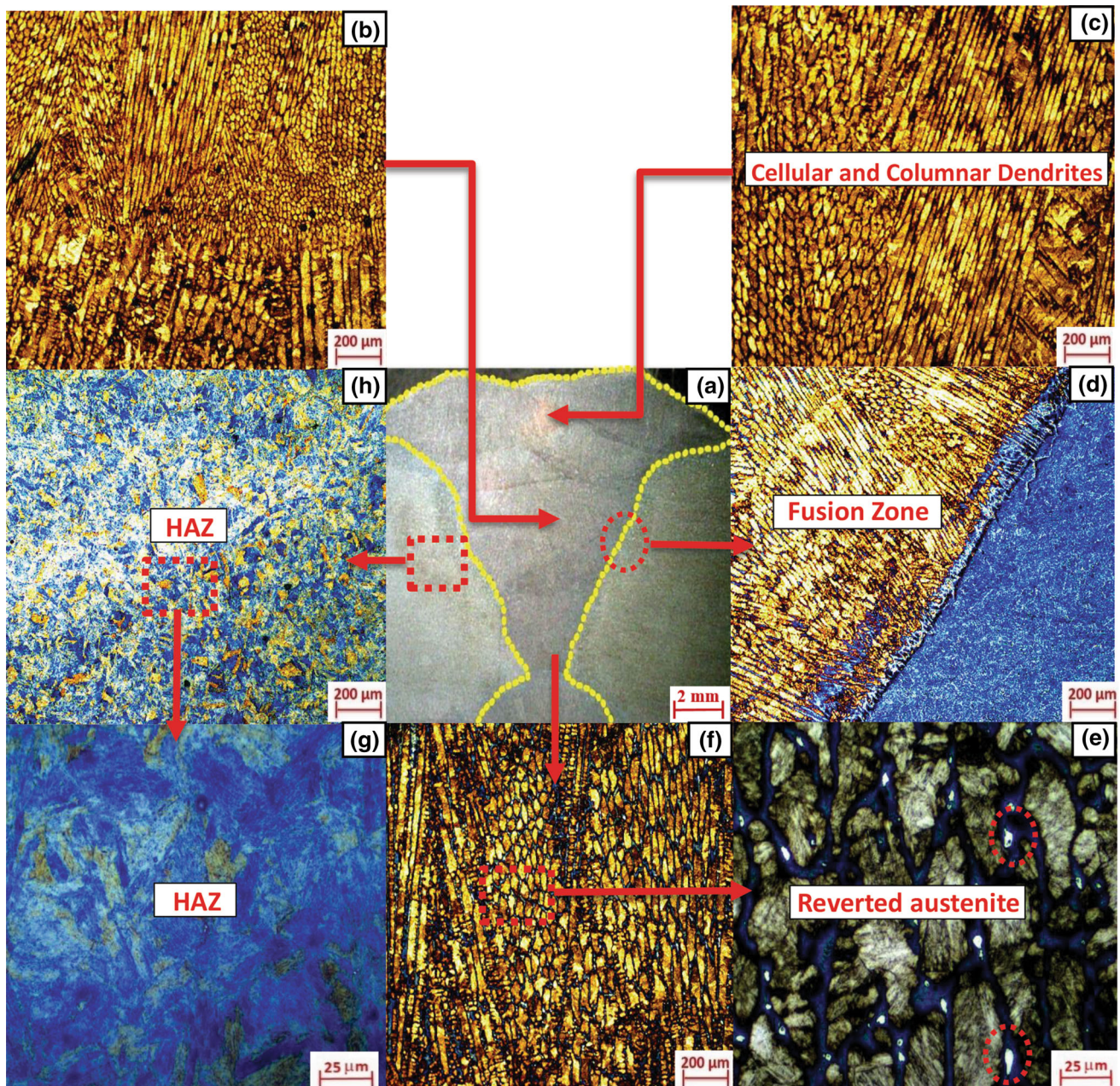


Fig. 6 (a-h) Macro and microstructure of SA condition

250 grade maraging steel. Furthermore, the precipitation reactions occur during the aging of the weld metal, contributes to hardening. It is widely assumed that the initial precipitation in MDN 250 grade maraging steel at 480 °C occurs as Ni_3Mo , which is replaced by Fe_2Mo after prolonged aging (Ref 20). Solutionizing treatment at 815 °C resulted in a reduction of Ni, Mo and Ti concentration at the cell boundaries. Since solutionizing temperature is greater than the austenitizing temperature, elements can dissolve to some extent into the matrix. This eventually reduced the austenite content in SA condition. However, homogenizing treatment at 1150 °C could completely even out segregation. Since homogenizing temper-

ature is greater than the austenite recrystallization temperature, the elements that had segregated to the cell boundaries during welding were re-dissolved into the matrix. Which led to the complete elimination of RA.

3.3 XRD Analysis

The XRD analysis were performed in the FZ of as-welded and PWHT conditions, as depicted in Figure 9. The XRD pattern of the as-welded condition reveal peaks corresponding to α Fe-Ni martensite (BCC). However, relative to the weld metal, post-weld aging appears another peak corresponding to

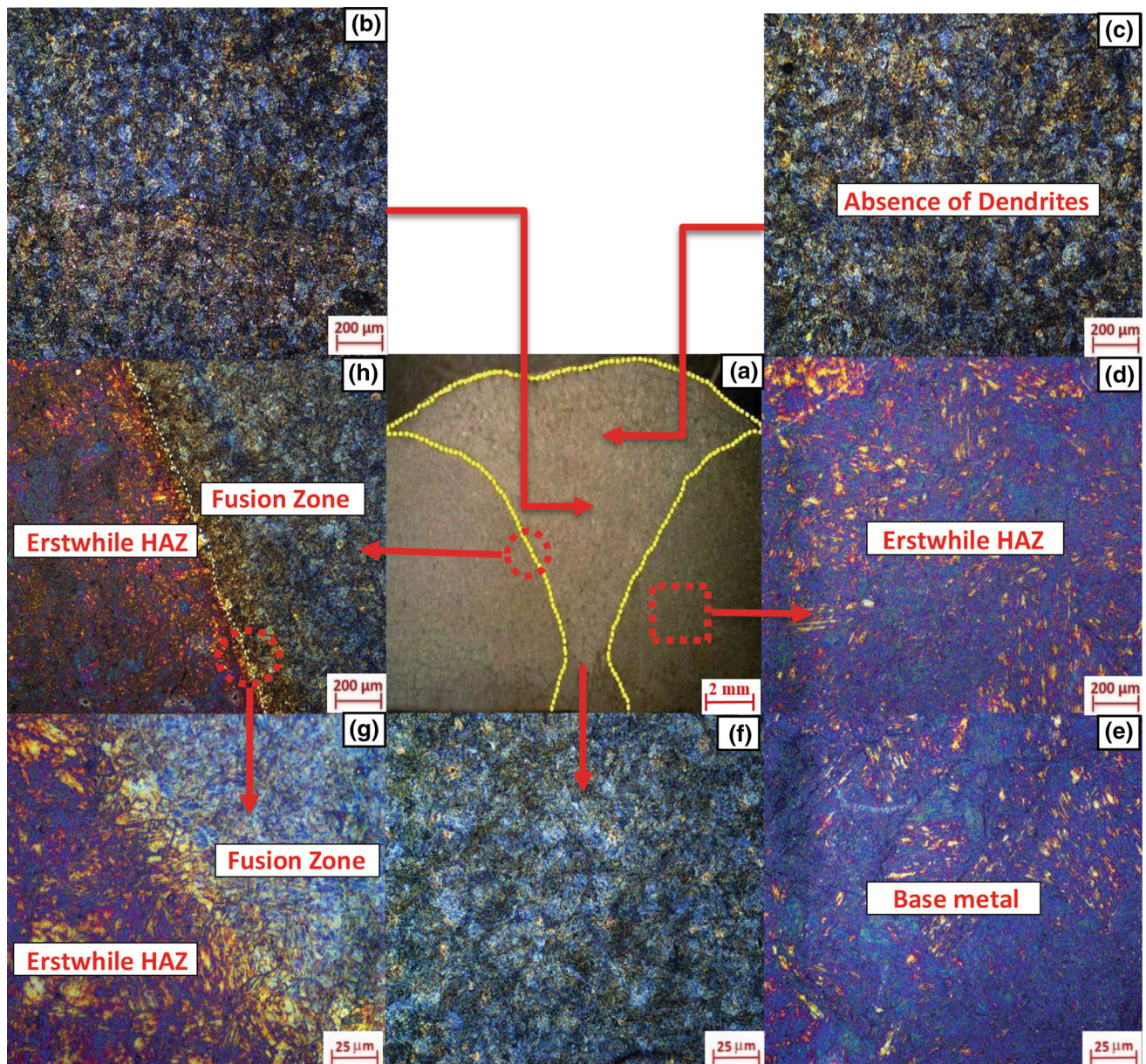


Fig. 7 (a-h) Macro and microstructure of HSA condition

γ -austenite (FCC). This γ austenite signifies the presence of RA in the FZ. The intensities of the precipitate peaks (Ni_3Ti , Fe_2Mo and Ni_3Mo) were found indistinguishable. This is because of the low volume fraction of precipitate particles, peak overlaps and also due to the close similarities in structure and d-spacing. The XRD pattern of the SA condition also resembles to that of DA condition with peaks of α -martensite and γ -austenite. However, in the case of HSA condition the presence of γ -austenite peaks were absent, which is in line with the EDS analysis. Peak shifts occur in XRD as a result of thermal treatments and changes in internal micro-strains (Ref 27). The XRD peak shifts are depicted in Figure 10. In the as-welded condition, the α -peak with maximum intensity was observed at 44.4 degrees. In the case of DA condition, the peak has taken a

positive shift to the right with 45.6 degrees. However, in the case of SA and HSA this shift was reduced to 45.4 and 45.1, respectively. The shifts in the peaks were observed due to PWHTs. However, DA shows a larger shift ($2\theta = 1.2^\circ$) which is due to the micro-strain caused by the precipitation of Ni_3 (Mo, Ti) and the formation of RA.

3.4 Electron Backscatter Diffraction

EBSD orientation map of as-welded and different PWHTs is depicted in Figure 11 (a–d). As shown in Figure 11(a), the grains showed a preferred orientation of $\{101\}$ in the inverse pole figure (IPF) of the as-welded condition. Since, martensite formation is easier along $\{101\}$ orientations from the habit

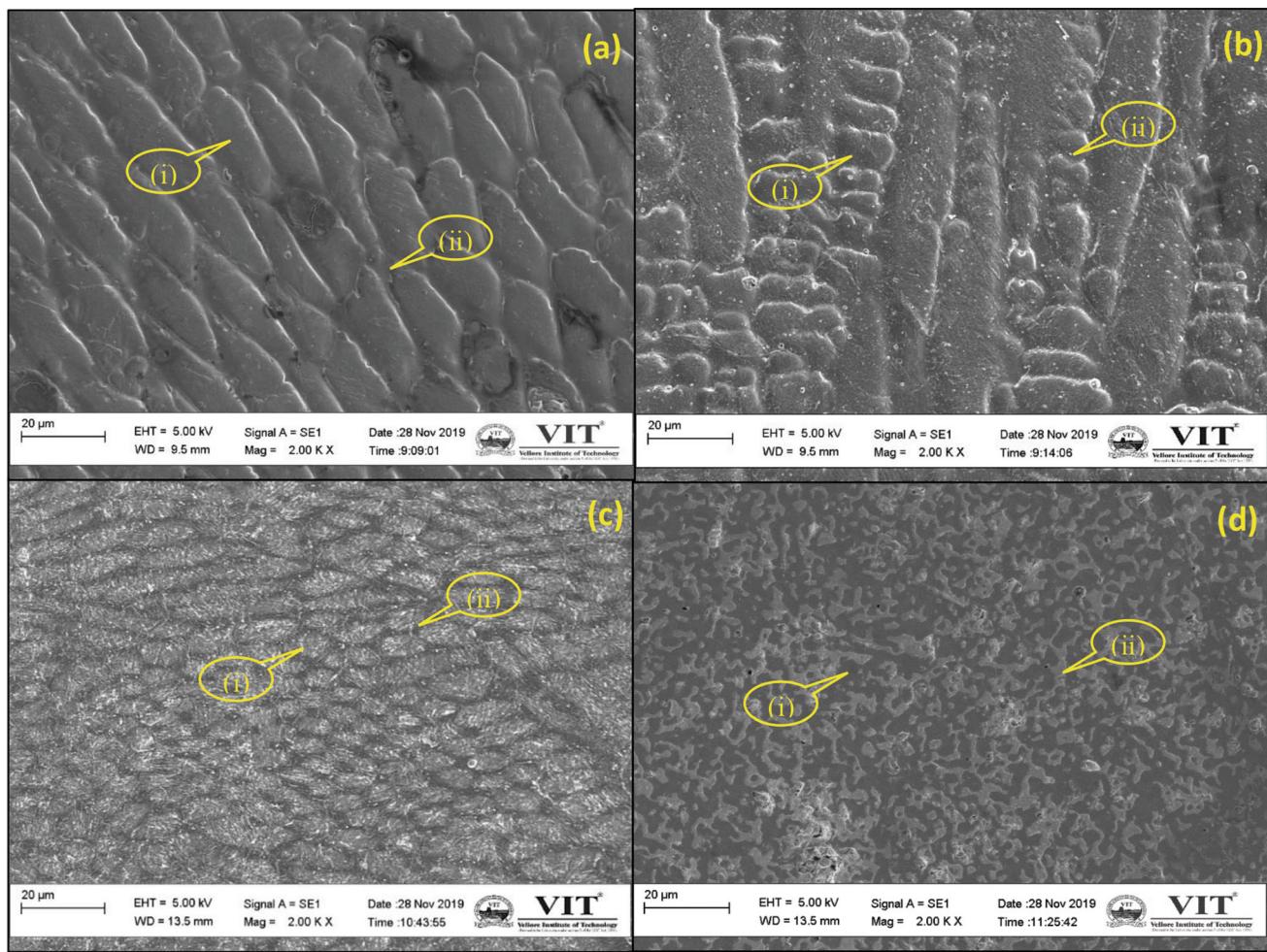


Fig. 8 SEM analysis of (a) as-welded sample, (b) DA, (c) SA and (d) HSA conditions

Table 3 EDS analysis of as-welded and different PWHT conditions

Sample Condition	Location	Ni	Mo	Co	Ti	Al	Fe
As-Welded	Cell center (i)	17.6	2.7	11.6	0.1	0.2	67.7
	Cell boundary (ii)	18.7	4.1	11.4	0.3	0.4	65
DA	Cell center (i)	17.4	2.3	11.5	0.2	0.3	68.2
	Cell boundary (ii)	18.6	4.2	11.3	0.3	0.4	65.1
SA	Cell center (i)	17.8	2.4	11.6	0.2	0.3	67.6
	Cell boundary (ii)	18.3	3.2	11.5	0.3	0.4	66.2
HSA	Cell center (i)	17.5	3.2	11.4	0.2	0.3	67.3
	Cell boundary (ii)	17.5	3.1	11.4	0.2	0.3	67.4
Bulk composition of fusion zone		17.9	2.6	11.4	0.2	0.3	67.5

planes $\{111\}$ of austenite during cooling (Ref 28). However, with different PWHTs, the preferred orientation weakened and became more random. Figure 12 (a–d) shows the grain size distribution of as-welded and PWHT conditions. The grain size distribution of as-welded, DA and SA conditions are in the range of $5 \mu\text{m} - 18 \mu\text{m}$. However, in the case of HSA, the grain size distribution ranges from $5 \mu\text{m} - 22 \mu\text{m}$. The high-temperature homogenization treatment has contributed to the increase in grain size, when compared to other conditions.

EBSD Phase map of as-welded and different PWHTs is depicted in Figure 13 (a–d). The EDS analysis confirmed the enrichment of alloying elements in the cell boundaries after welding. So during post-weld aging these alloy enriched sites are prone to austenite reversion. The XRD analysis confirmed that the DA indicates not only the martensite phase, but also the austenite phase. To get a better understanding of this phenomenon, the EBSD phase maps were performed. The phase map represents FCC austenite in green color and BCC ferrite

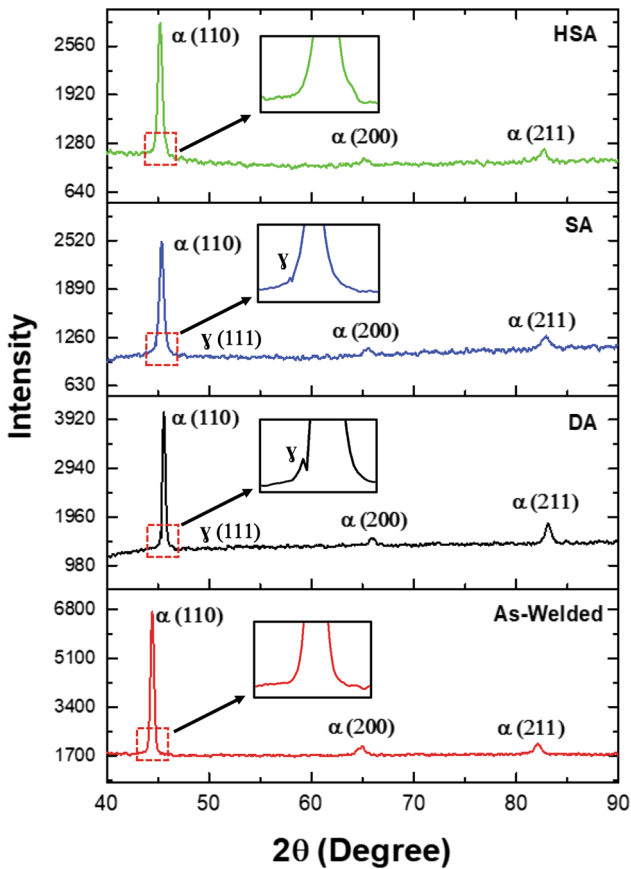


Fig. 9 XRD analysis of as-welded and PWHT conditions

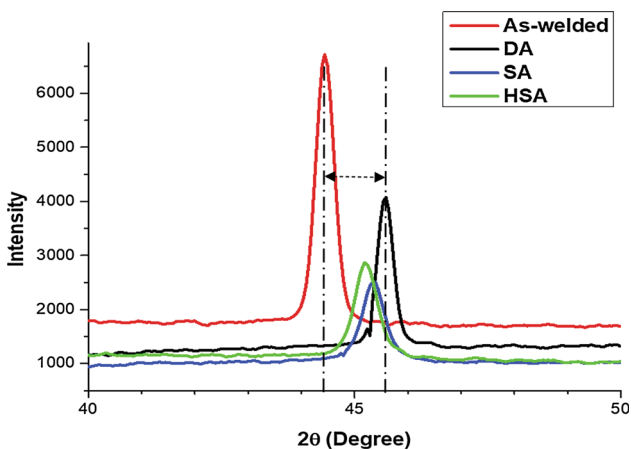


Fig. 10 XRD peak shift in as-welded and PWHT conditions

(martensite) in red color. As aforementioned, the as-welded condition was free from RA. In DA condition, the presence of RA pools were prominent. It was also observed that austenite pools were concentrated in the grain boundary. However, SA treatment shows a reduction in the presence of RA when compared to DA condition. HSA treatment was totally free from RA.

The variations in dislocation behavior can also be seen as a result of “Kernel average misorientation” (KAM) analyzed by EBSD (Ref 28). It is calculated by taking the average misorientation between each pixel and its nearest neighbors. KAM is used to represent the distribution of local strain or local dislocation density. These types of dislocation are associated with the “Geometry Necessary Dislocation” (Ref 29). KAM map of as-welded and different PWHTs is depicted in Figure 14 (a–d). From the KAM maps, it is clear that DA condition shows a higher degree of misorientation when compared to other conditions.

Figure 15 shows the plot of KAM distribution of as-welded and PWHT conditions. KAM plot of as-welded and HSA conditions reveals coinciding peaks with maxima distribution. It implies that both as-welded and HSA condition show the lowest degree of misorientation which is due to its single-phase structure. The KAM distribution peak was slightly shifted to the right in the case of DA condition, with decreased peak fraction and broadened distribution. This is due to the two-phase structure with higher amount of RA. This also confirms the presence of micro-strain in DA condition which was evident from the XRD analysis. However, SA condition shows a lower degree of misorientation when compared to DA condition.

3.5 Tensile Test

The transverse tensile tests were performed as per the ASTM E8 standard (Ref 30). Three distinct specimens were tested in each condition to ensure proper validation. The tensile properties of the base metal, as-welded and PWHTs are presented in Table 4. The photographs of fractured tensile samples of as-welded and PWHT conditions are shown in Figure 16 (a–d). The base metal in the solution-annealed condition shows a yield strength (YS) of 990 MPa and UTS of 1135 MPa. The strength of as-welded samples also indicates a similar trend as that of the base metal, which implies good joint efficiency. The failure of the as-welded samples occurred at a region away from the FZ; which is the base metal region. The PWHTs show a significant improvement in tensile properties when compared to the as-welded condition. This increase in tensile strength is attributed to the age-hardening reaction of martensite in the case of maraging steel weldments. The DA treatment shows an improvement of 24% in YS and 21% in the UTS when compared to the as-welded condition. However, the highest values of tensile properties were associated with SA condition, with YS of 1490 MPa and UTS of 1597 MPa. A similar observation was drawn by Fanton et al. (Ref 19) in a related work on laser welding of maraging steel. This increase in strength is due to the reduction of RA in the FZ as observed in Figure 13 (c). The HSA treatment on the other hand shows a similar trend as compared to SA treatment with a marginal reduction (about 1%) in the tensile property. Although the complete removal of RA did not increase the tensile strength considerably. However, this reduction in strength is due to the high-temperature homogenisation at 1150 °C that has given sufficient time for grain growth, which is evident from the EBSD analysis. As grain size increases, there is a reduction in strength as per the Hall-Petch relationship. However, when compared to the as-welded condition, the PWHT conditions exhibit a decrease in ductility. Since, ductility is mostly depend on matrix-strength and its flow characteristics, so the reduction

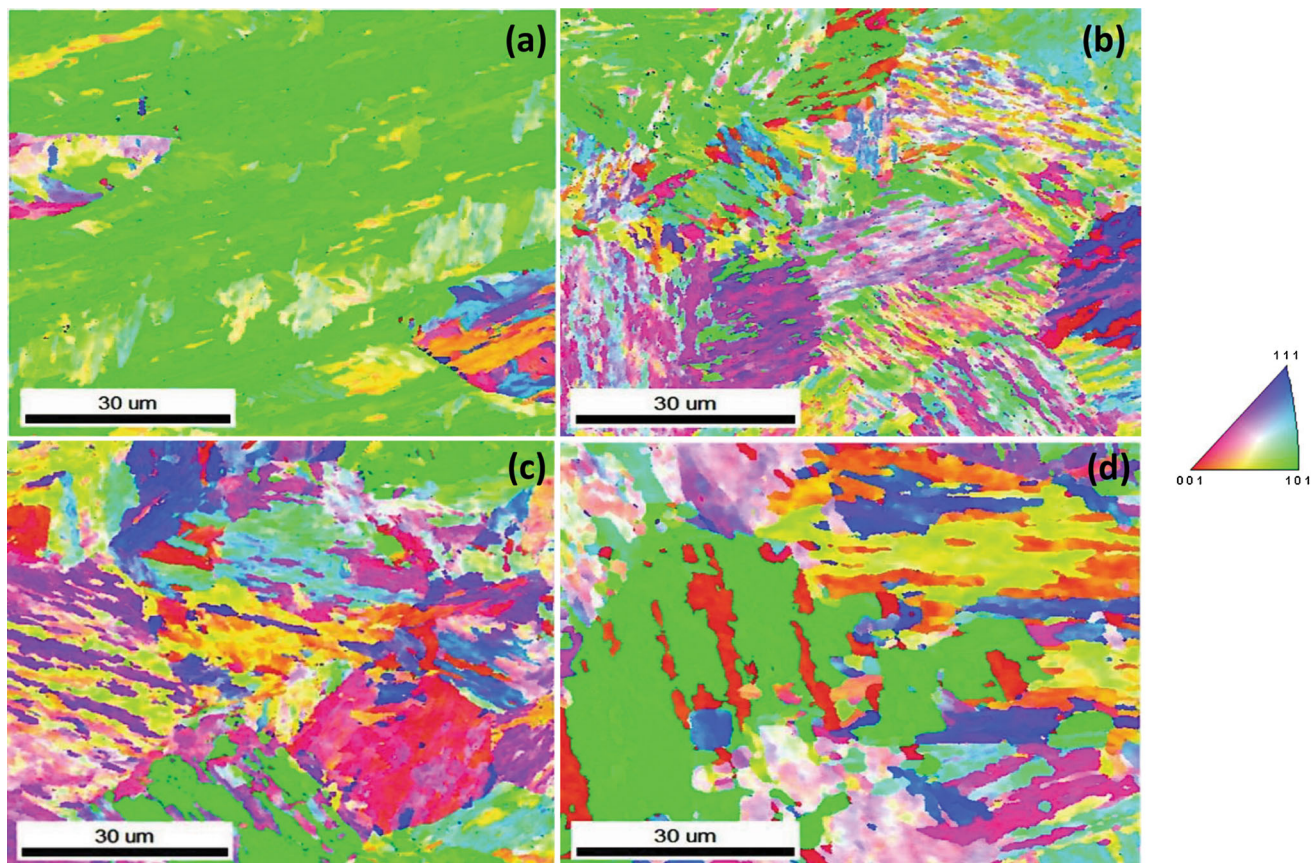


Fig. 11 Inverse pole figure of (a) as-welded, (b) DA, (c) SA and (d) HSA conditions

in ductility is majorly due to the precipitation reaction of the strengthening precipitates. Among the different PWHTs, HSA shows an improvement in tensile ductility, which is due to the absence of RA. It is also observed that all the PWHT samples failed in the FZ.

3.6 Fractography

Figure 17 (a-d) shows the tensile fractograph of as-welded and PWHT conditions. In each condition, the macrograph of the fractured surface is also depicted. In the as-welded condition, the failure occurred at the base metal region. The macrograph of the fractured surface resembles a cup and cone type of failure. The fractography of the as-welded samples also reveals the presence of large dimples, which signifies a ductile mode of failure. Figure 17 (b) shows the fractography of the DA condition. The macrograph showed a fracture devoid of necking with the failure occurred in the FZ. The yellow dotted line in the macrograph represents the FZ. The fractography of the DA condition shows micro-cracks and voids which is due to the combined action of precipitation and austenite reversion. The growth of these micro-cracks, which ultimately leads to the decrease in the strength and toughness of the welded joint. The mode of failure in DA condition resembles to brittle fracture. Figure 17 (c) and (d) shows the fractography of SA and HSA conditions. In both cases, fracture occurred at the FZ. The

macrograph shows brittle-like and a quasi-cleavage fracture mechanism. Whereas, the SEM fractograph revealed dimple which resembles to the ductile mode of failure. It was also observed that the dimples grew broader, deeper and fewer. So, in general terms SA and HSA show a mixed mode of failure.

3.7 Fracture Toughness

The fracture toughness tests were performed as per the ASTM E399 standard (Ref 31). To evaluate the fracture toughness K_{Ic} , a CT specimen with a straight notch was chosen. Figure 18 shows a schematic of fracture toughness specimen. In all the samples, the notch and the fatigue pre-crack were made at the center of the FZ which is longitudinal to the weld i.e., the crack plane having T-L orientation. The fracture toughness of the as-welded and different PWHTs are presented in Table 5. In the as-welded condition, the fracture toughness of the sample was 91.9 MPa√m. However, the DA condition shows a reduction of nearly 10% in fracture toughness when compared to as-welded condition. This reduction of fracture toughness is due to the presence of RA in the FZ. The RA being the softer phase compared to the martensite matrix, deforms preferentially and acts as sites for crack nucleation, which eventually sets a series of micro-cracks in the harder martensite matrix which ultimately leads to the reduction in toughness. SA condition, on the other hand, shows a reduction of about 6% in fracture

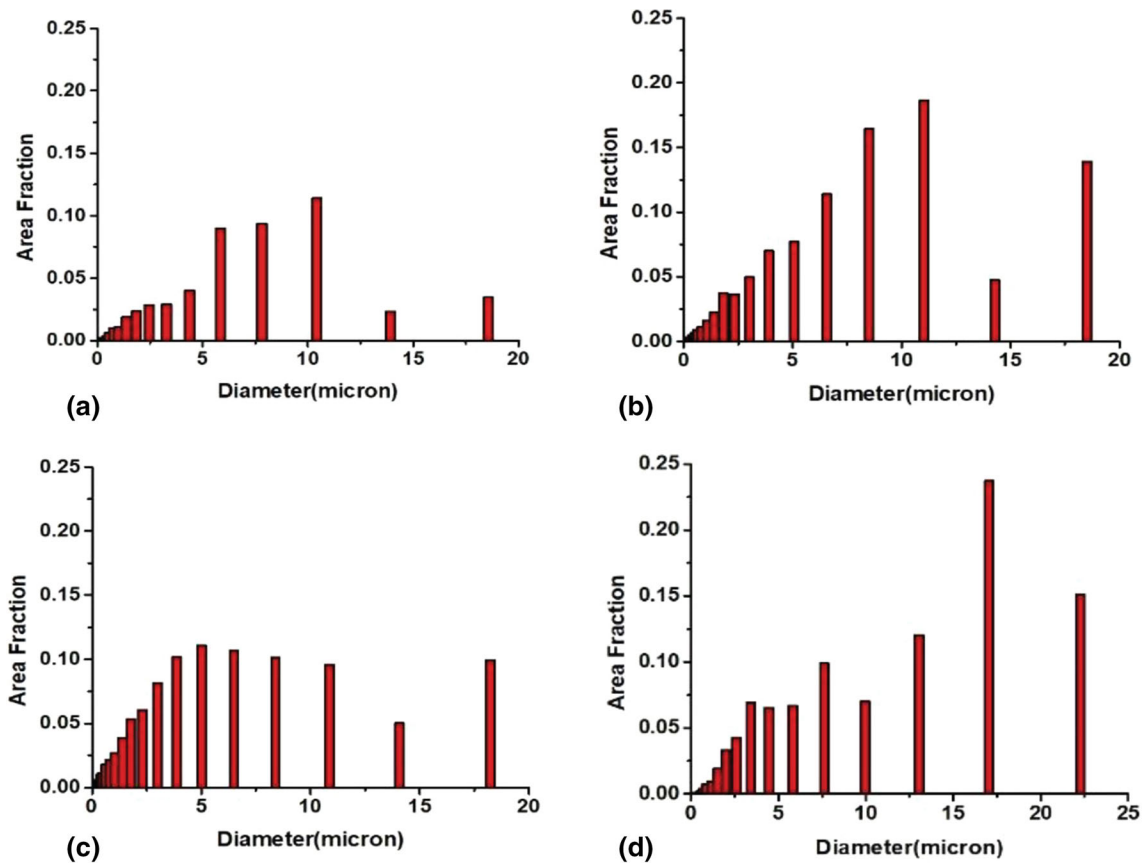


Fig. 12 Grain size distribution of (a) as-welded, (b) DA, (c) SA and (d) HSA conditions

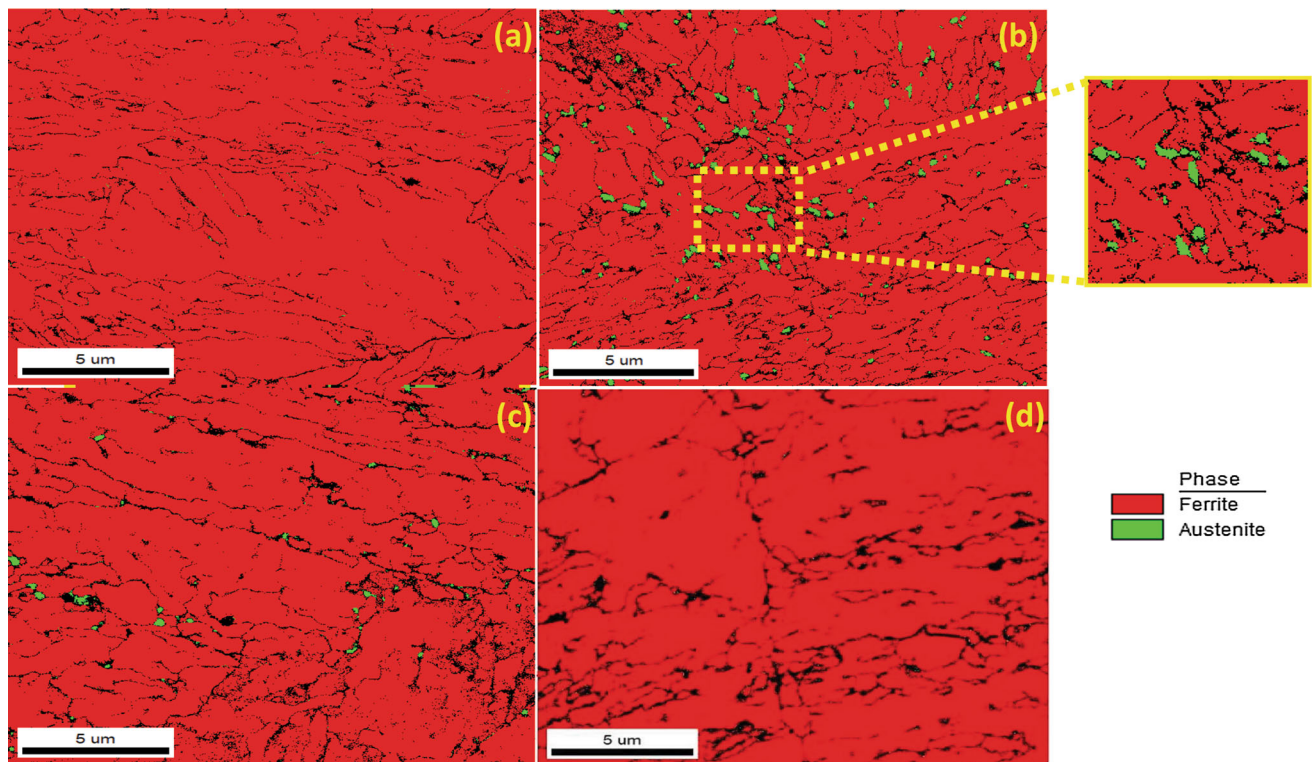


Fig. 13 Phase map of (a) as-welded sample, (b) DA, (c) SA and (d) HSA conditions

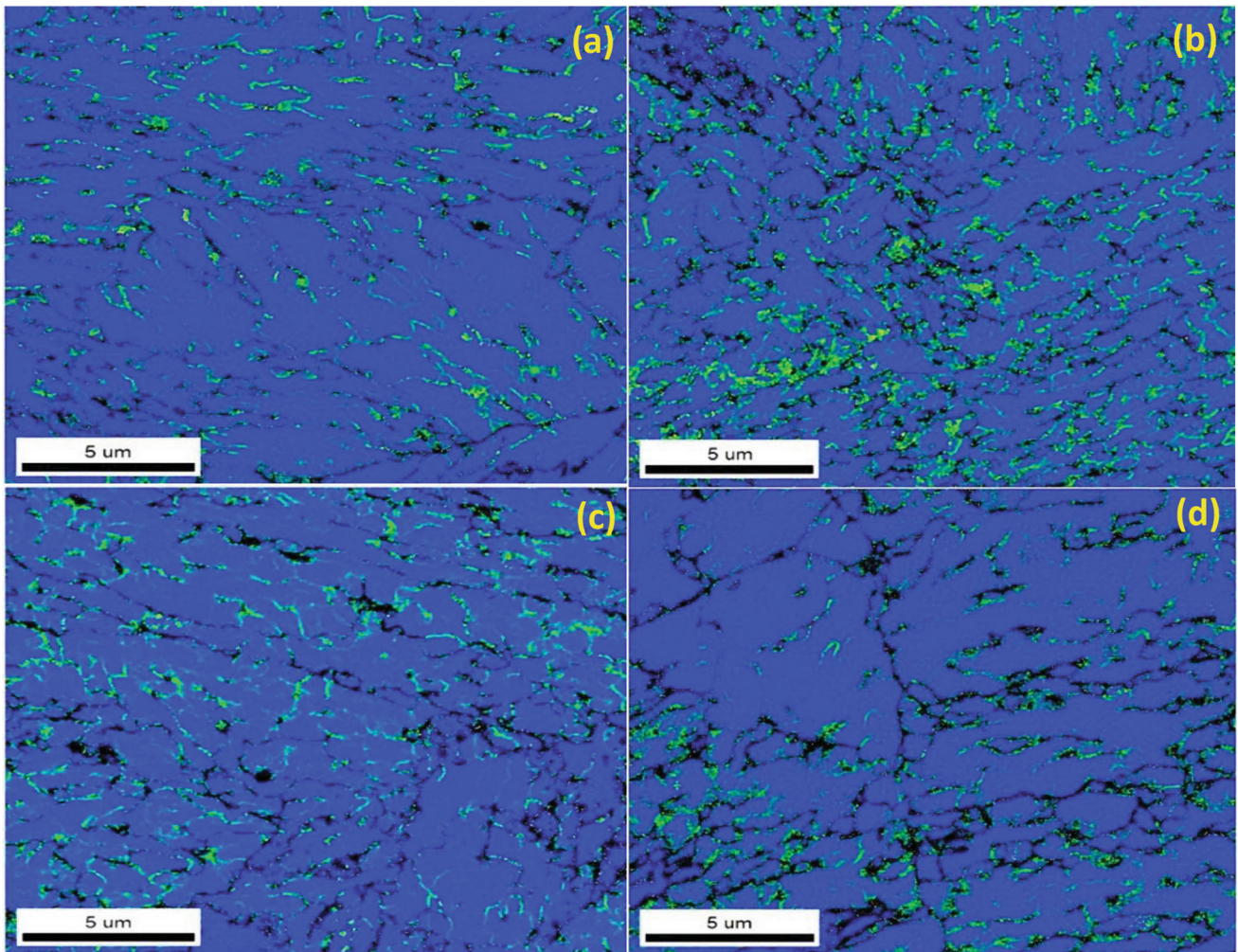


Fig. 14 KAM map of (a) as-welded sample, (b) DA, (c) SA and (d) HSA conditions

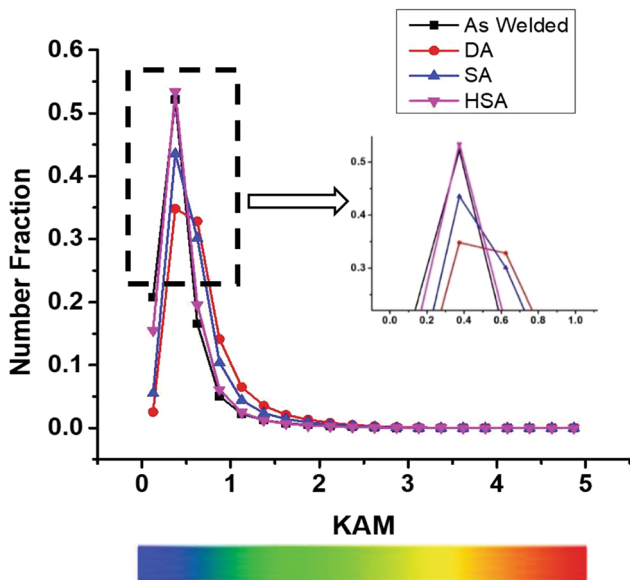


Fig. 15 KAM distribution of as-welded and PWHT conditions

Table 4 Tensile properties of the base metal, as-welded and different PWHT conditions

Materials	UTS , MPa	0.2 % Proof Strength , MPa	Elongation , %	Fracture Zone
Base Metal	1135	990	20	
As-Welded	1126	975	15	Base Metal
DA	1364	1211	8	Weld Zone
SA	1597	1490	8	Weld Zone
HSA	1582	1470	9	Weld Zone

toughness when compared to the as-welded condition, which is better when compared to DA condition. However, HSA treatment shows the maximum fracture toughness of 92.9 MPa√m. This value is even greater than the as-welded condition. The increase in the fracture toughness properties in the case of HSA treatment is due to the absence of RA in the

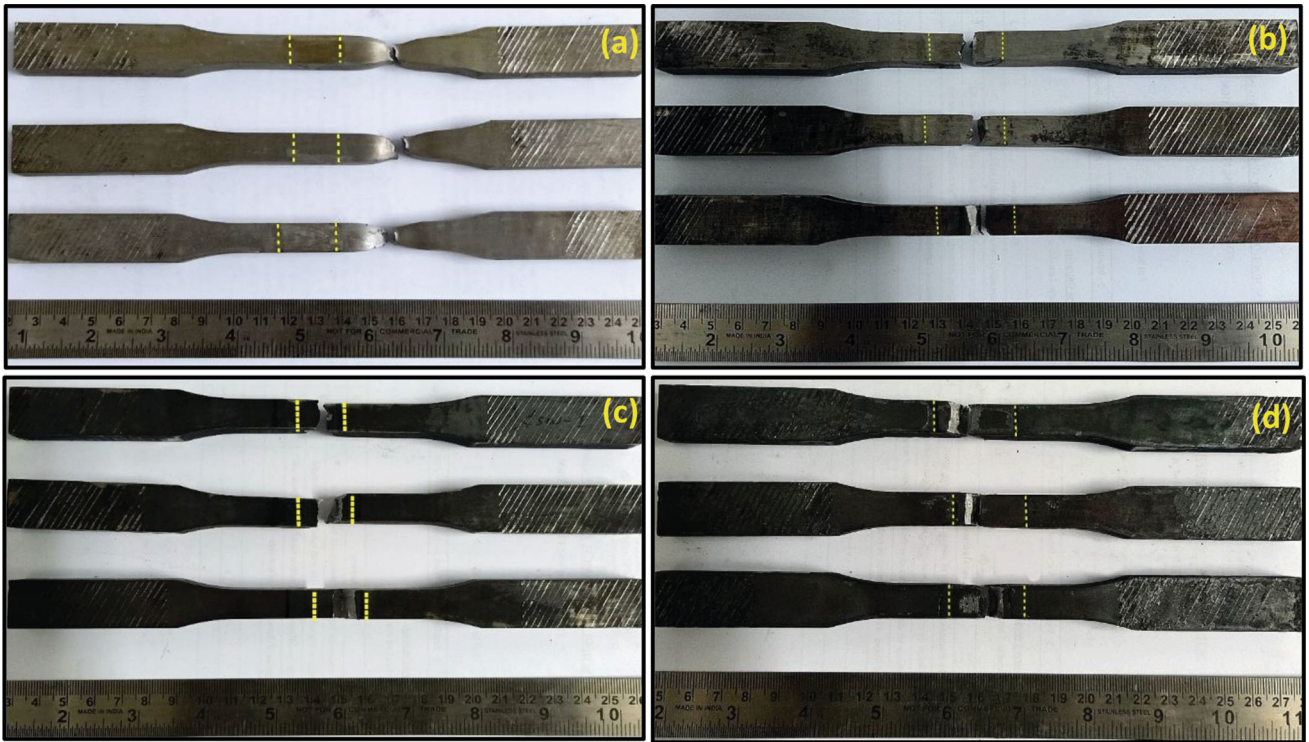


Fig. 16 Photograph of fractured tensile samples of (a) as-welded sample, (b) DA, (c) SA and (d) HSA condition

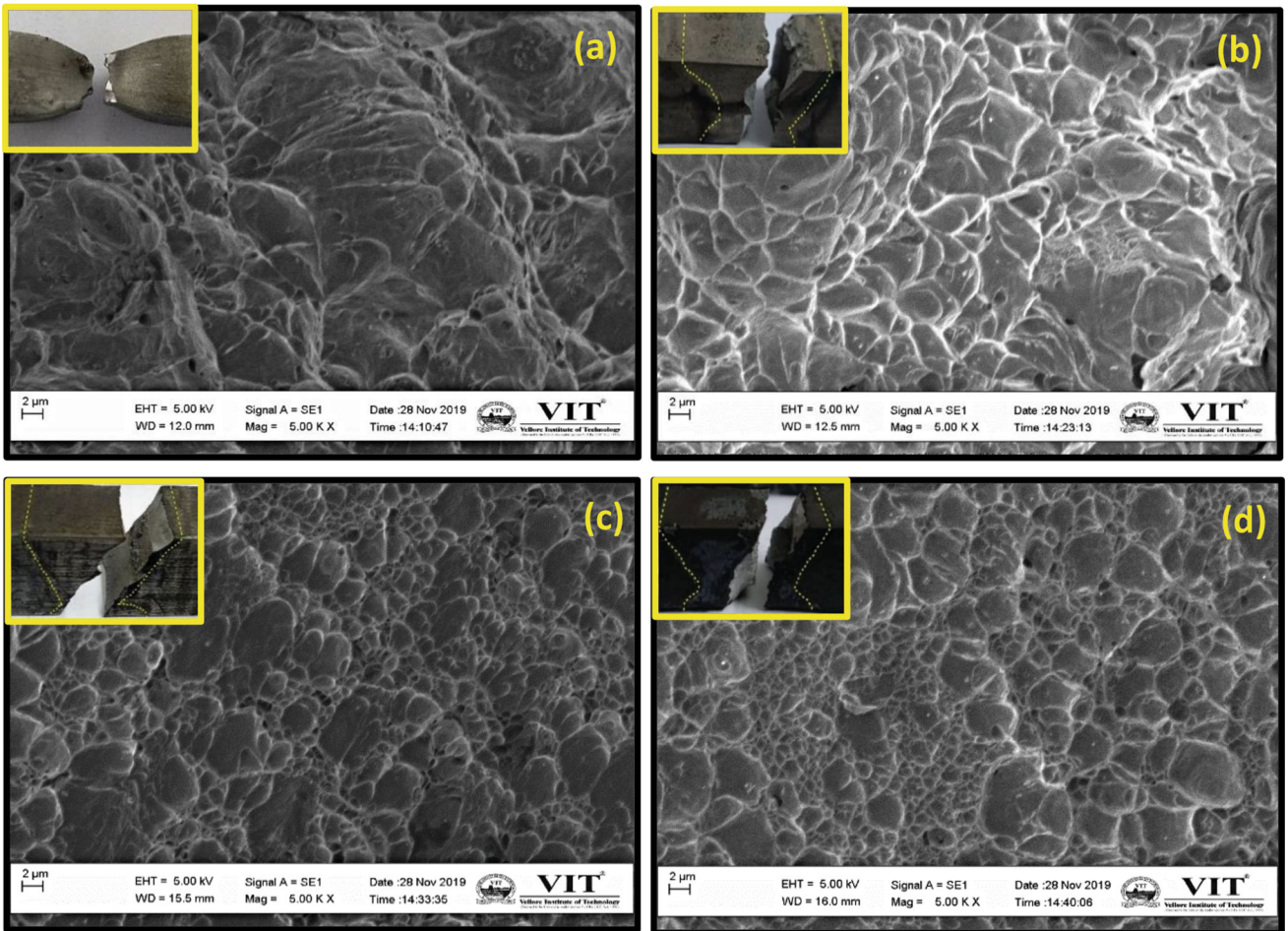


Fig. 17 Fractography of (a) as-welded sample, (b) DA, (c) SA and (d) HSA conditions

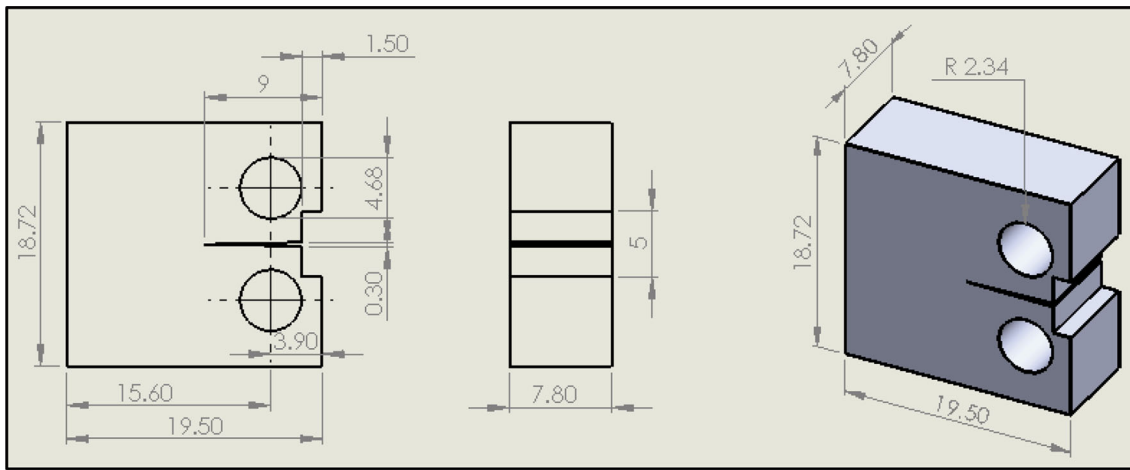


Fig. 18 Schematic of fracture toughness specimen

Table 5 Fracture toughness of as-welded and different PWHT conditions

Material	K_{Ic} (MPa \sqrt{m})
As-Welded	91.9
DA	82.8
SA	86.1
HSA	92.9

matrix as observed in Figure 13 (d). It can also be observed that in all the cases the fracture toughness value was more than 80 MPa \sqrt{m} which is very much acceptable for the aerospace applications.

3.8 Hardness

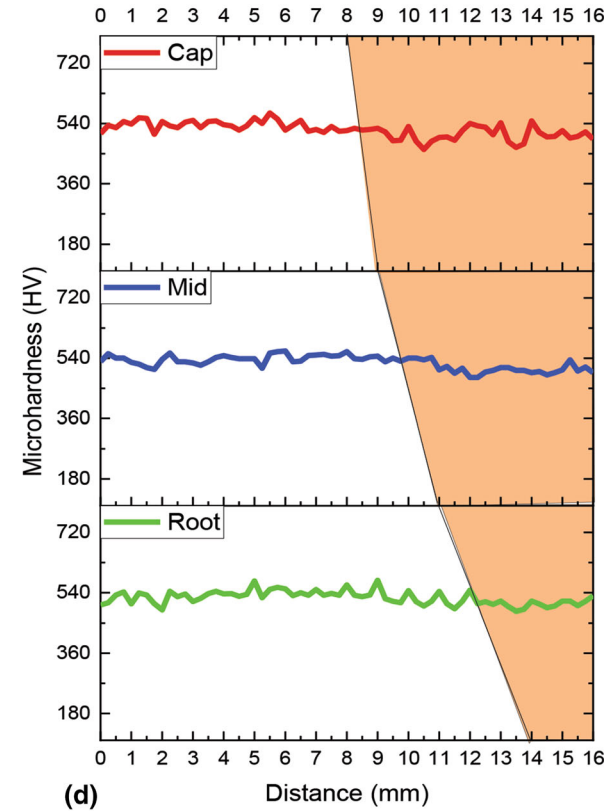
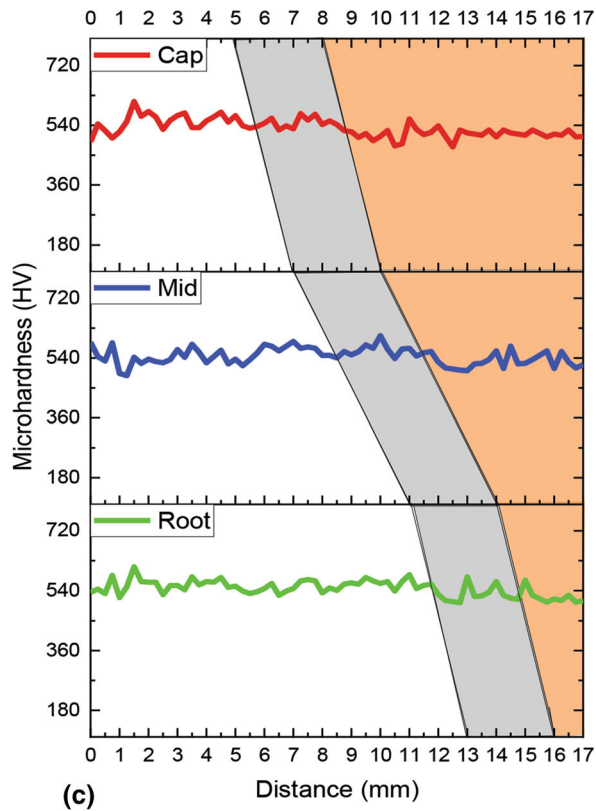
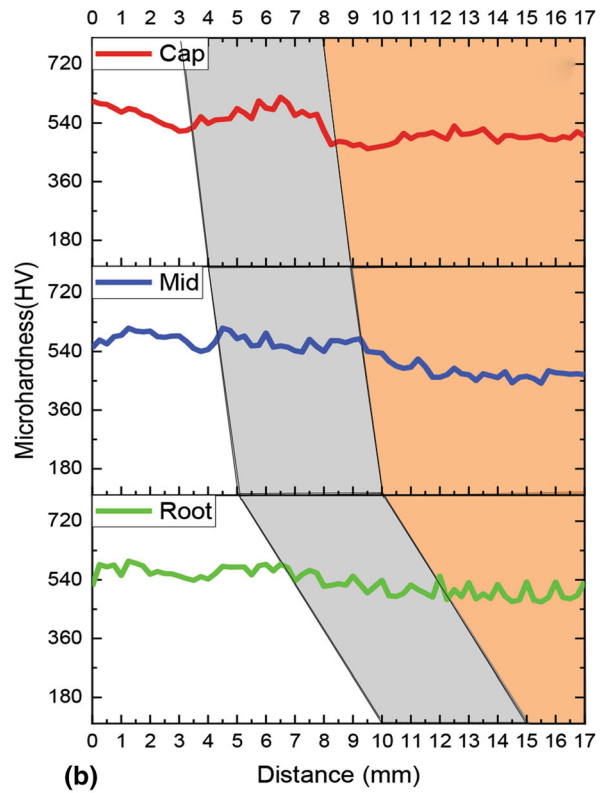
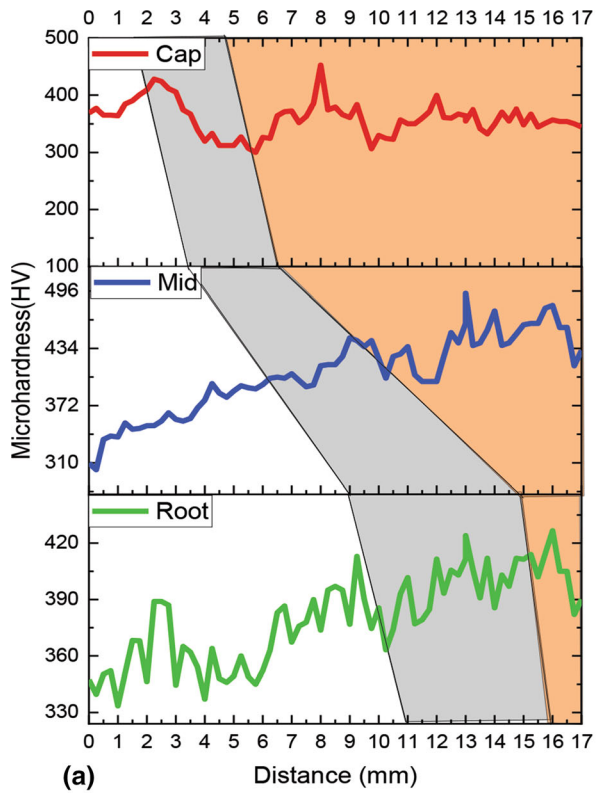
The influence of thermal cycle during welding plays a crucial role in the variation of hardness in the case of welded joints. The schematic representation of microhardness distributions in the as-welded and PWHT conditions are depicted in Figure 19. Error bars for microhardness in as-welded and different PWHT conditions are depicted in Figure 20. The microhardness analysis was performed in the transverse cross-section of the weldments. In each sample, the hardness was measured at three different locations starting with the cap region at the top, the mid-region at the center and in the root region at the bottom at an interval of 3 mm. Table 6 shows the average hardness distribution across the weldments.

Figure 19 (a) shows the microhardness of the as-welded condition. In the as-welded condition, the average hardness of the FZ and HAZ is higher than the base metal. So, this observation is in line with the tensile test result, as the fracture of the as-welded samples was observed in the base metal zone. The HAZ shown in the as-welded condition is a combination of both HAZ 1 and HAZ 2. Figure 19 (b) shows the microhardness of the DA condition. The aging has enhanced the hardness of the weldments by precipitation reaction. In the DA condition, the highest hardness was associated with the base metal region, and the lowest hardness was associated with the

FZ. This reduction in hardness is due to the presence of RA as observed in Figure 13 (b), which is soft when compared to the matrix. In the DA condition, also HAZ is a combination of both HAZ 1 and HAZ 2. Figure 19 (c) shows the microhardness of the SA condition. In the SA condition, the highest hardness was associated with the HAZ region, and the lowest hardness was associated with the FZ. However, when comparing the FZ hardness of DA and SA conditions, SA condition shows an improvement in the FZ hardness. This is due to the reduction of RA in the FZ. As revealed from the macro and microstructural analysis of the SA condition, the dark etched portion of HAZ has been completely dissolved into the martensite matrix. So, this is the reason why SA treatment yields a finer HAZ when compared to as-welded and DA conditions. Figure 19 (d) shows the microhardness of the HSA condition. The HSA shows an even trend in the hardness profile of the weldments. Here the FZ shows a marginal reduction in hardness compared to the rest of the weldment. In the HSA condition, it is not possible to distinguish between the base metal and the HAZ region. In all the post-weld heat-treated conditions, the FZ is the weakest region, which justifies the failure of tensile samples in the FZ.

4. Conclusions

1. The MDN 250 plate of 12-mm-thickness was effectively welded by multi-pass GMAW.
2. The microstructure of the FZ reveals cellular and columnar dendritic structure in the case of as-welded, DA and SA conditions. However, the dendrites were absent in the HSA condition.
3. The EDS analysis of the as-welded FZ revealed segregation of nickel, molybdenum and titanium along the cell boundaries. This resulted in the premature formation of RA on subsequent aging. The degree of segregation was greatest in the DA condition. While, SA treatments reduced segregation, HSA treatments completely eliminated segregation.



Fusion Zone
 HAZ
 Base Metal

Fig. 19 Microhardness of (a) as-welded sample, (b) DA, (c) SA and (d) HSA conditions

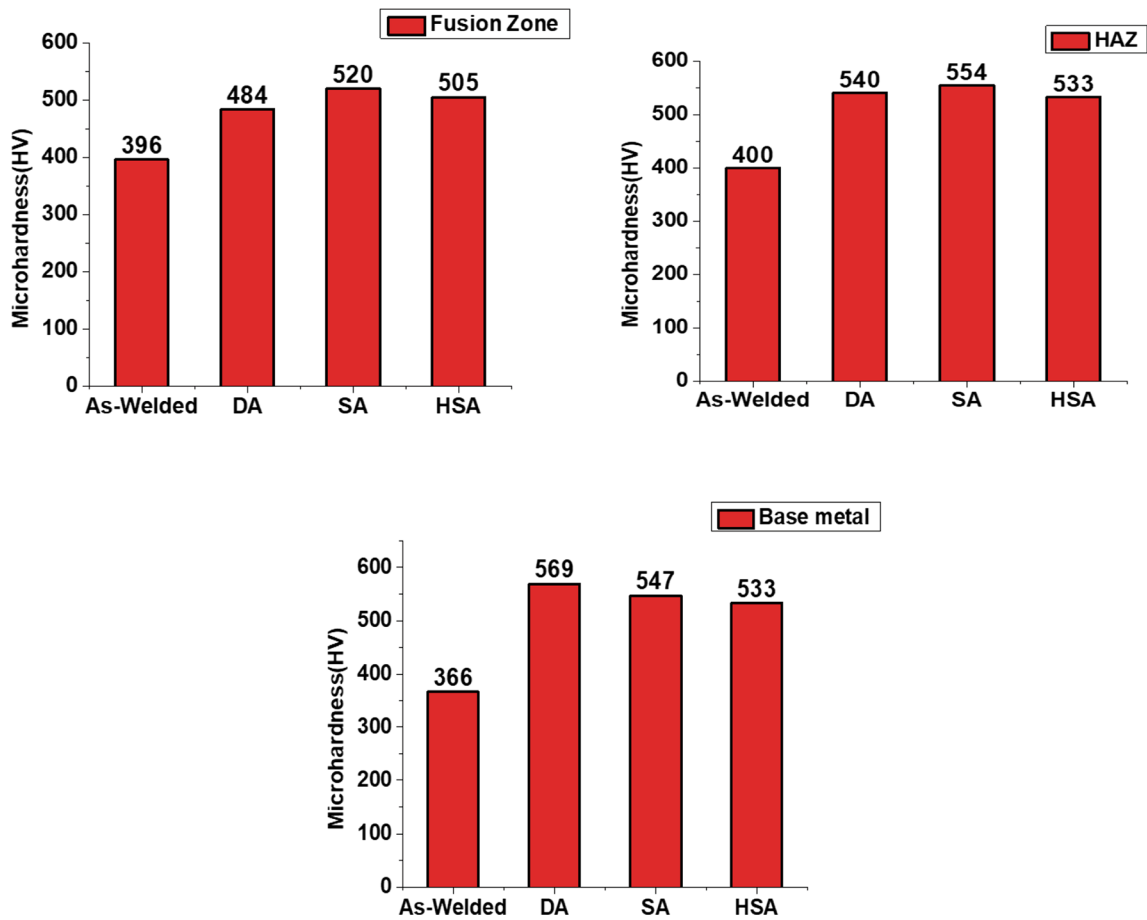


Fig. 20 Error bars for microhardness in as-welded and different PWHT conditions

Table 6 Average microhardness of as-welded and different PWHT conditions

Materials	Fusion Zone (HV)	HAZ (HV)	Base metal (HV)
As-Welded	396	400	366
DA	484	540	569
SA	520	554	547
HSA	505	533	533

- The microstructures of the post-weld heat-treated DA and SA treatments show the presence of RA in the cell boundary. Further, the presence of RA was confirmed by the XRD and EBSD analysis. However, RA was not observed in the case of HSA condition.
- The EBSD results revealed that the grains in the as-welded condition show a preferred orientation. However, with different PWHTs, the orientation became relatively more random.
- Among the different PWHTs, the highest degree of Kernel average misorientation was associated with DA condition, and the lowest was in the case of HSA condition.
- SA treatment shows the highest tensile properties; YS of 1490 MPa and a UTS of 1597 MPa. Which was followed by HSA, with YS of 1470 MPa and a UTS of 1582 MPa.

- The highest fracture toughness was observed in the HSA condition with a K_{Ic} value of 92.9 MPa \sqrt{m} . The fracture toughness of the FZ, in the order of its K_{Ic} values HSA > as-welded > SA > DA conditions.
- The maximum FZ hardness of 520 HV was obtained in the SA condition. However, HSA resulted in uniform distribution of hardness throughout the weldment.
- While taking into account of all the properties discussed, HSA treatments demonstrate optimal mechanical properties in GMAW welding of MDN 250 grade maraging steel.

Acknowledgment

We would like to convey our gratitude and thanks to DRDO, India, for providing financial assistance in carrying out this project. The authors are thankful to Dr. Nageswara Rao Muktinutalapati, Senior Professor, Vellore Institute of Technology for his continued guidance and encouragement. The authors also thank MIDHANI, Hyderabad, for carrying out the fracture toughness testing.

Funding

This research work was supported by the DRDO, India, (Grant No ERIP/ER/201705007/M/01/1727).

Conflict of interest

The authors declare that they have no conflict of interest.

References

1. R.F. Decker, C.J. Novak and T.W. Landig, Developments, and Projected Trends in Maraging Steels, *JOM*, 1967, **19**, p 60–66.
2. W. Sha and Z. Gwa, Introduction to Maraging Steels, *Maraging Steels*, 1st, Ed., Woodhead Publishing, 2009, p 1–16
3. M.N. Rao, Progress in Understanding the Metallurgy of 18 % Nickel Maraging Steels, *Int. J. Mater. Res.*, 2006, **97**(11), p 1594–1607.
4. L. Subashini, K.V.P. Prabhakar, S. Ghosh, and G. Padmanabham, Comparison of Laser-MIG Hybrid and Autogenous Laser Welding of M250 Maraging Steel Thick Sections — Understanding the Role of Filler Wire Addition, *Int. J. Adv. Manuf. Technol.*, The International Journal of Advanced Manufacturing Technology, 2020, (3–4)
5. A. O'Brien and C. Guzman, High-Alloy Steels, *AWS Welding handbook, Mater. Appl. Part*, 2011, **1**, p 95–135.
6. Z. Hu, D. Mo, C. Wang, G. He and C. Chen, Different Behavior in Electron Beam Welding of 18 Ni Co-Free Maraging Steels, *J. Mater. Eng. Perform.*, 2008, **17**, p 767–771.
7. D. feng MO, Z. fei HU, S. juan CHEN, C. xu WANG, and G. qiu HE, (2009) Microstructure and Hardness of T250 Maraging Steel in Heat Affected Zone, *J. Iron Steel Res. Int.*, Central Iron and Steel Research Institute, **16**(1): 87–91
8. Y. Lee, I. Lee, S. Wu, M. Kung and C. Chou, Effect of Post-Weld Heat Treatments on Microstructure and Mechanical Properties of Electron Beam Welded Flow Formed Maraging Steel Weldment, *Sci. Technol. Weld. Join.*, 2007, **12**(3), p 266–274.
9. S.D. Meshram, G. Madhusudhan Reddy, and S. Pandey, Friction Stir Welding of Maraging Steel (Grade-250), *Mater. Des.*, Elsevier Ltd, 2013, **49**, p 58–64
10. S.D. Meshram, A.G. Paradkar, G.M. Reddy, and S. Pandey, Friction Stir Welding: An Alternative to Fusion Welding for Better Stress Corrosion Cracking Resistance of Maraging Steel, *J. Manuf. Process.*, The Society of Manufacturing Engineers, 2017, **25**, p 94–103
11. S.D. Meshram, A.G. Paradkar, G.M. Reddy, and S. Pandey, “Stress Corrosion Cracking Behaviour of Gas Tungsten Arc and Friction Stir Maraging Steel Welds,” *Materials Today: Proceedings*, Elsevier Ltd, 2018, p 26968–26973
12. G.M. Reddy, V. V Rao, and A.V.S. Raju, “The Effect of Post-Weld Heat Treatments on the Microstructure and Mechanical Properties of Maraging Steel Laser Weldments,” *Proceedings of the Institution of Mechanical Engineers Part L Journal of Materials Design and Applications*, 2009, p 149–159
13. R. Karthikeyan and M. Saravanan, Effect of Heat Input and Post-Weld Heat Treatment on the Mechanical and Laser-Welded Maraging Steel Joints, *Surf. Rev. Lett.*, 2017, **24**(7), p 1–13.
14. K. Li, J. Shan, C. Wang, and Z. Tian, Influence of Aging Temperature on Strength and Toughness of Laser-Welded T-250 Maraging Steel Joint, *Mater. Sci. Eng. A*, Elsevier, 2016, **669**, p 58–65
15. R. Gupta, R. Reddy and M.K. Mukherjee, Key-Hole Plasma Arc Welding of 8 Mm Thick Maraging Steel – A Comparison with Multi-Pass GTAW, *Weld. World*, 2012, **56**, p 69–75.
16. L. Subashini, K.V.P. Prabhakar, R.C. Gundakaram, and S. Ghosh, Single Pass Laser-Arc Hybrid Welding of Maraging Steel Thick Sections Single Pass Laser-Arc Hybrid Welding of Maraging Steel Thick Sections, *Mater. Manuf. Process.*, Taylor & Francis, 2016, p 2186–2198
17. F.H. Lang and N. Kenyon, “Welding of Maraging Steels,” *Welding Research Council*, (New York), Welding Research Council, 1971
18. B. Rohit and N.R. Muktinatalapati, Austenite Reversion in 18% Ni Maraging Steel and Its Weldments, *Mater. Sci. Technol.*, 2018, **34**(3), p 253–260.
19. L. Fanton, A.J. Abdalla and S. Fernandes, Heat Treatment and Yb-Fiber Laser Welding of a Maraging Steel, *Weld. Res.*, 2014, **93**, p 362–368.
20. C.R. Shamantha, R. Narayanan, K.J.L. Iyer, V.M. Radhakrishnan, S.K. Seshadri, S. Sundararajan and S. Sundaresan, Microstructural Changes during Welding and Subsequent Heat Treatment of 18Ni (250-Grade) Maraging Steel, *Mater. Sci. Eng. A*, 2000, **287**(1), p 43–51.
21. G. Madhusudhan Reddy and K. Srinivasa Rao, Microstructure and Corrosion Behaviour of Gas Tungsten Arc Welds of Maraging Steel, *Def. Technol.*, Elsevier Ltd, 2015, **11**(1), p 48–55
22. V. Venkateswara Rao, G. Madhusudhan Reddy, and A. V. Sitarama Raju, Influence of Post-Weld Heat Treatments on Microstructure and Mechanical Properties of Gas Tungsten Arc Maraging Steel Weldments, *Mater. Sci. Technol.*, 2010, **26**(12), p 1459–1468
23. K. Li, J. Shan, C. Wang, and Z. Tian, Effect of Post-Weld Heat Treatments on Strength and Toughness Behavior of T-250 Maraging Steel Welded by Laser Beam, *Mater. Sci. Eng. A*, Elsevier, 2016, **663**, p 157–165
24. V. Rajkumar and N. Arivazhagan, Role of Pulsed Current on Metallurgical and Mechanical Properties of Dissimilar Metal Gas Tungsten Arc Welding of Maraging Steel to Low Alloy Steel, *J. Mater.*, Elsevier Ltd, 2014, **63**, p 69–82
25. S. Kou, “Welding Metallurgy,” *JOHN WILEY & SONS*, 2003
26. F. Tariq, R.A. Baloch, B. Ahmed and N. Naz, Investigation into Microstructures of Maraging Steel 250 Weldments and Effect of Post-Weld Heat Treatments, *J. Mater. Eng. Perform.*, 2010, **19**(2), p 264–273.
27. M. Sathishkumar, M. Manikandan, and N. Arivazhagan, Prospects of Pulsed Current Arc Welding on Aerospace Grade Hastelloy X, *Proc. Inst. Mech. Eng. Part E J. Process Mech. Eng.*, 2021
28. K. Li, L. Wei, B. An, B. Yu and R.D.K. Misra, Aging Phenomenon in Low Lattice-Misfit Cobalt-Free Maraging Steel: Microstructural Evolution and Strengthening Behavior, *Mater. Sci. Eng. A*, 2019, **2019**(739), p 445–454.
29. S.I. Wright, M.M. Nowell and D.P. Field, A Review of Strain Analysis Using Electron Backscatter Diffraction, *Microsc. Microanal.*, 2011, **17**(3), p 316–329.
30. ASTM E8 / E8M-16a₁, “Standard Test Methods for Tension Testing of Metallic Materials,” (West Conshohocken, PA), 2016
31. ASTM E399-90, “Standard Test Method for Plane-Strain Fracture Toughness of Metallic Materials,” (West Conshohocken, PA), 1997

Publisher's Note Springer Nature remains neutral with regard to jurisdictional claims in published maps and institutional affiliations.